

A Novel Spoke-Type PM Machine Employing Asymmetric Modular Consequent-Pole Rotor

J. Li[✉], Student Member, IEEE, and K. Wang[✉], Senior Member, IEEE

Abstract—This paper proposes a novel spoke-type permanent magnet (PM) machine, which adopts asymmetric modular consequent-pole (AMCP) rotor to enhance the effective PM flux due to the increased flux-focusing effect and reduced leakage flux and to improve the flux-weakening capability due to the increased *d*-axis inductance. Moreover, the pole-shaping method based on three sectional arcs is proposed to suppress the harmonics of airgap flux density. Since the rotor structure is relatively complex, the finite-element analysis together with multiobjective genetic algorithm is adopted to optimize this design. Furthermore, the electromagnetic performance of the spoke-type PM machine with the proposed AMCP rotor (Spoke-AMCP), including the open-circuit airgap flux density, phase back electromotive force, torque, PM utilization ratio, efficiency, and flux-weakening capability, are compared with two conventional spoke-type PM machines with evenly distributed and alternate flux barriers (Spoke1 and Spoke2) and consequent-pole spoke-type PM machine (Spoke-CP). It is demonstrated that the Spoke-AMCP machine obtains the largest output torque and PM utilization ratio, lowest torque ripple and similar efficiency compared to Spoke1, Spoke2 and Spoke-CP machines. Moreover, although the Spoke-AMCP machine has the largest PM flux linkage, it has slightly better flux-weakening capability than the Spoke1 and Spoke2 machines. Finally, a 12-slot/10-pole Spoke-AMCP machine is built and tested to verify the analyses.

Index Terms—Alternate flux barrier, asymmetric rotor, flux-focusing effect, genetic algorithm (GA), leakage flux, modular consequent-pole, multiobjective optimization, spoke type.

I. INTRODUCTION

PERMANENT magnet (PM) machines are widely used in industry applications and electric vehicles because of the

Manuscript received December 28, 2018; revised April 26, 2019; accepted July 10, 2019. Date of publication July 30, 2019; date of current version October 15, 2019. Recommended by Technical Editor S. K. Dwivedi. This work was supported in part by the National Natural Science Foundation of China under Project 51607089, in part by the Natural Science Foundation of Jiangsu Province under Project BK20180016, in part by the Six Talent Peaks Project of Jiangsu Province under Grant 2017-XNYQC-015, in part by the Power Electronics Science and Education Development Program of the Delta Environmental and Educational Foundation under Grant DREK2019002, and in part by the Postgraduate Research & Practice Innovation Program of Jiangsu Province under Grant KYCX18_0284. (*Corresponding author: K. Wang.*)

The authors are with the College of Automation Engineering, Nanjing University of Aeronautics and Astronautics, Nanjing 211100, China (e-mail: jli@nuaa.edu.cn; k_wang@ieee.org).

Color versions of one or more of the figures in this paper are available online at <http://ieeexplore.ieee.org>.

Digital Object Identifier 10.1109/TMECH.2019.2931950

advantages of high torque/power density, high efficiency, and high power factor [1], [2]. According to the location of PMs in the rotor, PM machines can mainly be classified into two types—surface-mounted PM (SPM) machines and interior PM (IPM) machines. Generally, IPM machines have better flux-weakening capability, stronger rotor robustness, and lower risk of irreversible demagnetization than SPM machines [2].

PMs with high energy density (such as NdFeB) are favorable for these machines. However, their prices increase year by year due to the shortage and increasing demand. Therefore, many researchers strive for the development of less or no rare-earth PM machines [3]. One approach is to improve the PM material utilization ratio. In [4], the shape of interior PMs was designed to increase the torque density with minimal magnet volume, and the results show that the V-shaped IPM machine has higher PM utilization ratio than the bar-shaped one due to the flux-focusing effect of two PMs in one pole. In fact, the flux-focusing effect can be further enhanced by maximizing the depth of the V-shaped PM array, i.e., spoke-type PM array [5]–[9], which increases the airgap flux density and hence the output torque. Therefore, spoke-type PM machines become strong candidates for applications where both the PM utilization ratio and torque density are primary concerns [10].

Another one is to utilize low-cost PM material, such as ferrite PMs, which have considerable advantage of the cost [10]–[19]. However, although these machines adopt the spoke-type PM array for obtaining strong flux-focusing effect [10]–[17], or the PM-assisted synchronous reluctance rotor for utilizing reluctance torque [18], [19], they suffer from poor torque density.

In recent years, consequent-pole topology has attracted increasing attention due to the high PM utilization ratio, which has been widely studied in SPM machines with fractional-slot concentrated winding [20]–[23]. It was concluded that the CPM machine obtains the similar torque density to the conventional SPM machine because of the reduced equivalent reluctance and the improved fundamental airgap flux density by optimizing the PM-arc ratio [20], [21]. In [23], the dovetailed consequent-pole rotor was presented to reduce the cost of PM and sleeve in the SPM machine while the torque density and demagnetization withstand capability are improved. A consequent-pole IPM machine was investigated in [24]. Moreover, in [22] and [24], it has been concluded that the two CPM machines have wider constant power range than the conventional counterparts under rated on-load. In [25] and [26], the hybrid-pole rotors combining consequent-pole and spoke-type PM rotors are proposed to

eliminate the unipolar leakage flux without sacrificing the output torque and PM utilization ratio.

From above, the spoke-type PM machines may furtherly improve the PM utilization ratio by using the consequent-pole topology. Therefore, the consequent-pole spoke-type PM (Spoke-CP) machine was investigated in [27]–[29]. However, it is well known that the mechanical reliability of the conventional spoke-type PM machines is guaranteed by the supporting iron bridges and ribs, which result in leakage flux and, hence, reduce the PM utilization ratio and torque density. Therefore, the alternate flux barriers is proposed to reduce the leakage flux of the ribs in [28], and it is adopted in spoke-type vernier PM machines [30], [31]. However, the iron bridges and ribs still exist in the spoke-type PM rotors with consequent-pole topology and alternate flux barriers. Although various nonmagnetic supports are proposed in spoke-type machines to obtain sufficient mechanical strength as well as low flux leakage [6]–[8], [15], [19], they increase the manufacturing difficulties and incur additional costs.

Therefore, this paper proposes an asymmetric modular consequent-pole (AMCP) rotor to strength the flux-focusing effect and suppress the leakage flux by eliminating the flux bridges and ribs and, hence, improve the PM utilization ratio and torque density. Meanwhile, the flux-weakening capability is improved due to the increased d -axis inductance. Moreover, the pole-shaping-method-based three-sectional arcs are proposed to suppress the harmonics of airgap flux density and hence the torque ripple. Furthermore, the design is optimized by finite-element (FE) analysis coupled with multiobjective genetic algorithm (GA) and compared with three conventional Spoke-type PM machines. Finally, a prototype is fabricated to validate the foregoing analyses.

II. MACHINE WITH DIFFERENT SPOKE-TYPE PM ROTORS

A. Topologies

It has been concluded that the even-order harmonics can be eliminated in resultant phase back electromotive force (EMF) when $N_s/(mt)$ is even (t is the greatest common divisor of the stator slot number N_s and rotor pole-pair number p , and m is the phase number). Therefore, the 12-slot/10-pole combination is employed to investigate the electromagnetic performance of different spoke-type PM machines. Fig. 1(a) and (b) shows the conventional spoke-type PM rotors with evenly distributed and alternate flux barriers (i.e., Spoke1 and Spoke2), respectively. Fig. 1(c) shows the Spoke-CP rotor, which embeds the consequent-pole PMs to the alternate flux barriers of Spoke2. Fig. 1(d) shows the proposed spoke-type AMCP (Spoke-AMCP) rotor, which consist of main core, separated cores, and PMs. The “modular” is named because the rotor core is divided into the main core and separated cores.

In the existing Spoke1, Spoke2, and Spoke CP rotors, the flux bridges and ribs are needed to protect the PMs and iron-poles. In the Spoke-AMCP rotor, the PMs are locked inside the main rotor core by the separated cores. Therefore, the self-protection is achieved when the rotor is rotating. It should be noted that the flux per pole in the Spoke-AMCP rotor is produced by four

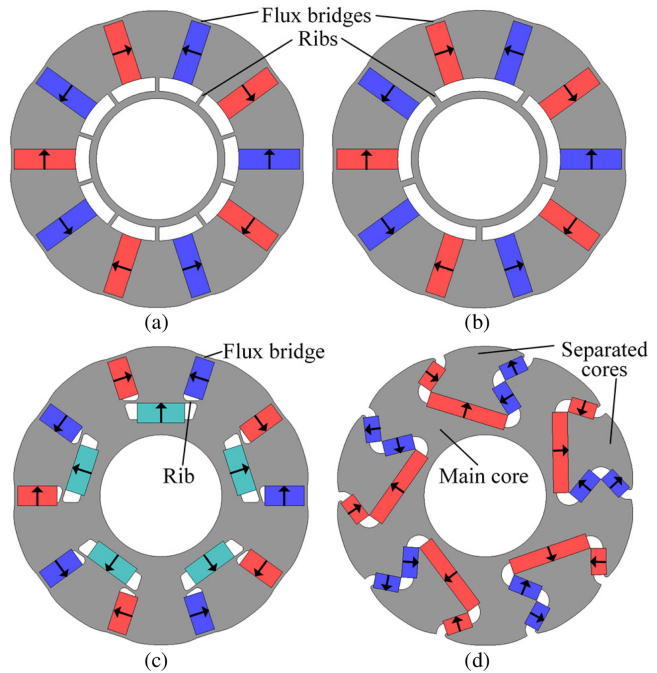


Fig. 1. Cross section of different Spoke-type PM rotors. (a) Conventional Spoke rotor (Spoke1). (b) Conventional Spoke rotor with alternate flux barriers (Spoke2). (c) Spoke rotor with consequent-pole PMs (Spoke-CP). (d) Novel asymmetric modular Spoke-CP rotor (Spoke-AMCP).

TABLE I
BASIC PARAMETERS OF 12-SLOT/10-POLE MACHINES

Parameters	Value	Unit
Number of phases	3	-
Stack length, L_s	51	mm
Stator outer radius, R_{so}	45	mm
Stator inner radius, R_{si}	25	mm
Rotor outer radius, R_{ro}	24.5	mm
Rotor inner radius, R_{ri}	10	mm
Minimum airgap length, g	0.5	mm
PM remanence(20°C)	1.2	T
PM relative permeability	1.05	-
Turns per coil	55	-
Rated phase current, I_r	3.6	A_{rms}
Rated speed, n_r	1500	rpm

PMs, which results in the strong flux-focusing effect. Moreover, the iron bridges and ribs do not exist in the Spoke-AMCP rotor, which results in the reduction of the leakage flux. Consequently, the Spoke-AMCP machine may has higher torque density and PM utilization ratio than the other three spoke-type PM machines. All the investigated machines have the same stator, stack length and airgap length, and the basic design parameters are given in Table I.

B. Design and Optimization

Although spoke-type PM machines have superior performance in terms of high torque density and PM utilization ratio, their airgap flux density have serious distortion, which will result in large torque ripple [16], [17]. Since the nonuniform airgap can

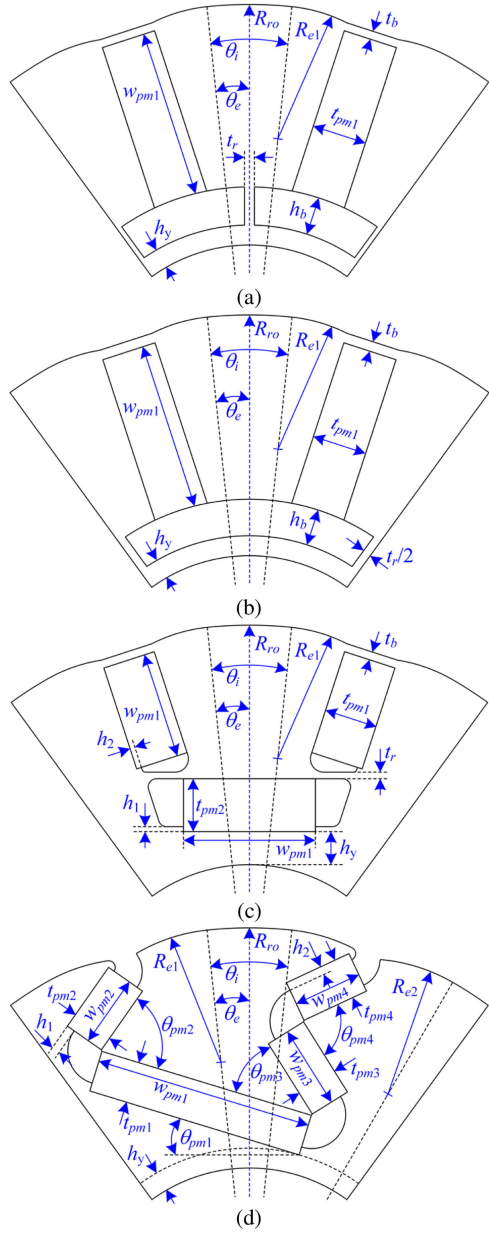


Fig. 2. Parametric models of rotors. (a) Spoke1. (b) Spoke2. (c) Spoke-CP. (d) Spoke-AMCP.

change the airgap permeability, the pole-shaping-method-based three sectional arcs are proposed to suppress the harmonics of the airgap flux density without decreasing the fundamental one. The detailed parametric models of these rotors are shown in Fig. 2. It can be seen that there are three sectional arcs in one pole-arc, in which the middle arc has the same radius as the rotor, and the bilateral arcs are eccentric. The eccentricity starts at the point of one-third pole-pitch θ_{pp} , i.e.,

$$\theta_i = 2\theta_e = \frac{1}{3}\theta_{pp}. \quad (1)$$

1) Spoke1, Spoke2, and Spoke-CP: Fig. 3(a) and (b) shows the variations of average torque and torque ripple with radius

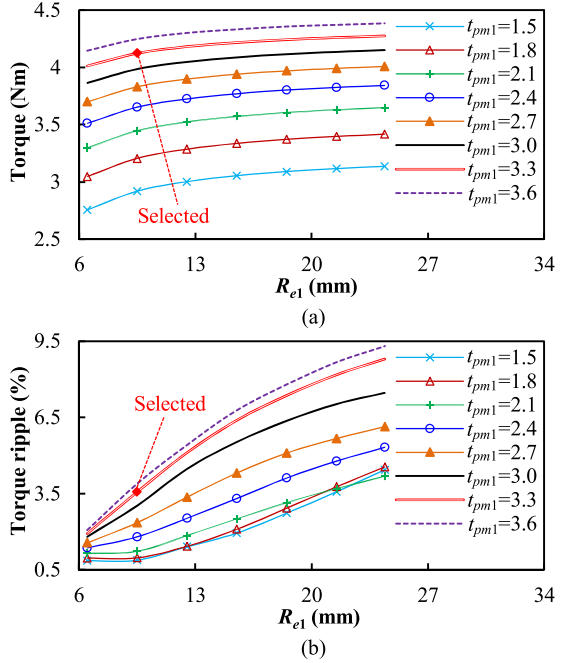


Fig. 3. Variations of average torque and torque ripple with R_{e1} and t_{pm1} for Spoke1. (a) Average torque. (b) Torque ripple.

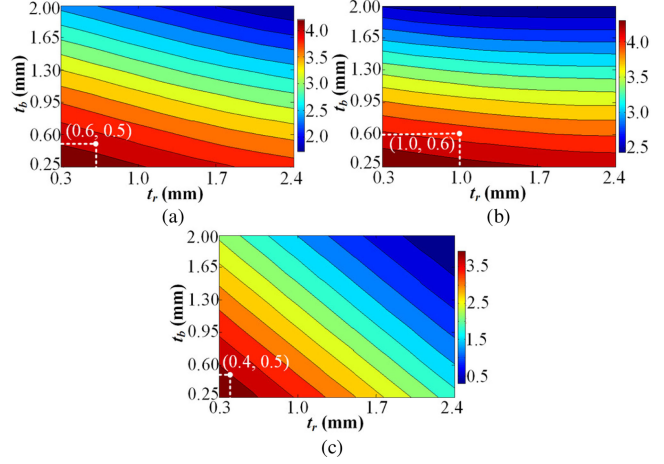


Fig. 4. Variations of average torque with t_r and t_b . (a) Spoke1. (b) Spoke2. (c) Spoke-CP.

of eccentric arc R_{e1} and PM thickness t_{pm1} in Spoke1, respectively. Apparently, both the average torque and torque ripple increase with R_{e1} . However, the increase in torque ripple is much larger than that of average torque, which indicates that the proposed pole-shaping method can suppress the torque ripple effectively with slight sacrifice of average torque. Fig. 4(a) shows the variation of average torque with the thickness of rib t_r and thickness of flux bridge t_b in Spoke1. The average torque decreases with both t_r and t_b due to the increased leakage flux while the mechanical reliability increases with them. From above, the key parameters of the Spoke1 rotor are determined in Table II, which is the baseline for the other rotors.

TABLE II
OPTIMIZATION RESULTS OF KEY PARAMETERS FOR EXISTING ROTORS

Items	Spoke1	Spoke2	Spoke-CP	Unit
t_b	0.5	0.6	0.5	mm
t_r	0.6	1	0.4	mm
h_y	1.2	1.2	2	mm
h_b	2.3	2.2	-	mm
$t_{pm1,2,3,4}$	3.3	3.3	3.2	mm
w_{pm1}	10.8	10.7	6.6	mm
w_{pm2}	-	-	7.7	mm
R_{el1}	9.5	9.5	9.5	mm
h_1	-	-	0.3	mm
h_2	-	-	0.3	mm

TABLE III
DESIGN PARAMETERS OF SPOKE-AMCP

Parameters	Variation rang	Unit
$pm1$	15~22	°
$pm2$	55~82	°
$pm3$	33~55	°
$pm4$	58~123	°
w_{pm1}	11~15	mm
w_{pm3}	4~6	mm
$R_{el1,2}$	1~15	mm
$h_{1,2}$	0.4~0.8	mm

Fig. 4(b) and (c) shows the variations of average torque with the thickness of rib t_r and thickness of flux bridge t_b in Spoke2 and Spoke-CP. It is similar to the Spoke1, both the average torques of Spoke2 and Spoke-CP decrease with t_r and t_b . However, the decrease with t_r in Spoke2 is less than that in Spoke1 and Spoke-CP due to the suppressed leakage flux by alternate flux barriers. Meanwhile, the decrease in t_r in Spoke-CP is larger than that in Spoke1 because the increase in t_r reduces the width of PM1 w_{pm1} . In addition, since the number of ribs in Spoke2 is half of that in Spoke1, the thickness of flux bridge t_b in Spoke2 should be larger than that in Spoke1 to maintain the similar mechanical strength. Consequently, the key parameters of the Spoke2 and Spoke-CP rotors are determined in Table II, which have the same PM volume as the Spoke1 rotor.

2) Spoke-AMCP: Due to the asymmetric modular structure, the Spoke-AMCP rotor have more geometric parameters than the other rotors. Moreover, the multiple design objectives (high output torque, low torque ripple, and PM volume) complicate the design process. Therefore, the FE analysis coupled with multiobjective GA is adopted to optimize the design. In order to guarantee the reliability of the mechanical structure and avoid the geometric conflict, ten key design parameters are chosen for the multiobjective optimization, and their range of variations are listed in Table III. In GA, the population is an assembly of elements that are calculated by FE analysis, and the number of elements in each population is named as population size. It should be noted that the large population size is time-consuming. As a tradeoff between accuracy and computational cost, the population size is set to 30. Moreover, the maximum generation number (36) is set to stop the optimization compulsively. The

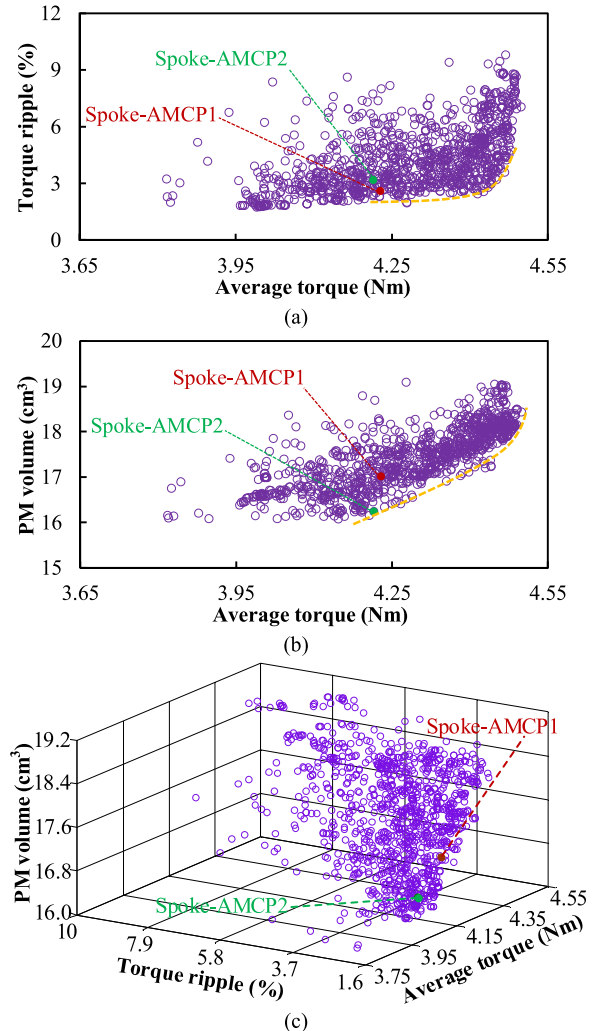


Fig. 5. Optimization results of Spoke-AMCP machine. (a) Average torque versus torque ripple. (b) Average torque versus PM volume. (c) Three-dimensional view of three objectives.

optimization problem is formulated as

$$\max \{f_1(x), -f_2(x), -f_3(x)\}, \quad x \in R \quad (2)$$

where x refers to the geometric parameters, R refers to their constraints, as shown in Table III, f_1 is the average torque, f_2 is the torque ripple, and f_3 is the PM volume.

Fig. 5(a) shows the optimized results of the average torque and torque ripple. There is no explicit relationship between them due to the complicated parameters. Fig. 5(b) shows the relationship between the average torque and the PM volume, and Fig. 5(c) shows the three-dimensional (3-D) view of the three objectives to show the results clearly. It can be observed that the average torque is positive correlated with the PM volume. Based on the tradeoff among the average torque, torque ripple, and PM volume, the Spoke-AMCP1 is selected, and its key parameters are listed in Table IV. It should be noted that the Spoke-AMCP1 has the same PM volume as the Spoke1, Spoke2, and Spoke-CP machines. In addition, the Spoke-AMCP2 is selected when the PM volume has the highest priority. Apparently, the Spoke-

TABLE IV
OPTIMIZATION RESULTS OF KEY PARAMETERS FOR SPOKE-AMCP

Items	Spoke-AMCP1	Spoke-AMCP2	Unit
t_b	-	-	mm
t_f	-	-	mm
h_y	1.2	1.2	mm
h_p	-	-	mm
$t_{pm1,2,3,4}$	2.5	2.5	mm
w_{pm1}	13.2	13	mm
w_{pm2}	4.3	3.3	mm
w_{pm3}	5	5.2	mm
w_{pm4}	4.2	4	mm
$\theta_{pm1,2,3,4}$	17/72/41/83	21/76/46/85	°
R_{e11}	10.5	9.8	mm
R_{e12}	10.5	14.5	mm
R_{e21}	10.5	10.8	mm
R_{e22}	10.5	11.5	mm
h_1	0.5	0.5	mm
h_2	0.5	0.5	mm

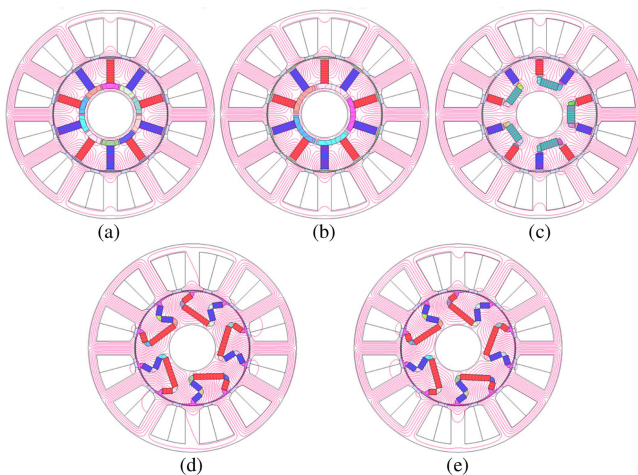


Fig. 6. Open-circuit flux lines. (a) Spoke1. (b) Spoke2. (c) Spoke-CP. (d) Spoke-AMCP1. (e) Spoke-AMCP2.

AMCP2 has lower PM volume than the Spoke-AMCP1, whereas it has slightly higher torque ripple and slight low average torque than the Spoke-AMCP1.

III. ELECTROMAGNETIC PERFORMANCE COMPARISON AND ANALYSIS

In the previous section, the investigated machines are introduced and optimized by FE analysis. In this section, the electromagnetic performances of the Spoke-AMCP machines are investigated and compared with those of the Spoke1, Spoke2, and Spoke-CP machines.

A. Open-Circuit Airgap Flux Density

FE-predicted open-circuit flux distributions of the five typical spoke-type PM machines are shown in Fig. 6, and their airgap flux density and corresponding harmonic contents are, respectively, shown in Fig. 7(a) and (b). It can be seen that the Spoke2 machine has slight lower fundamental airgap flux density (fifth) than the Spoke1 machine because it has thicker

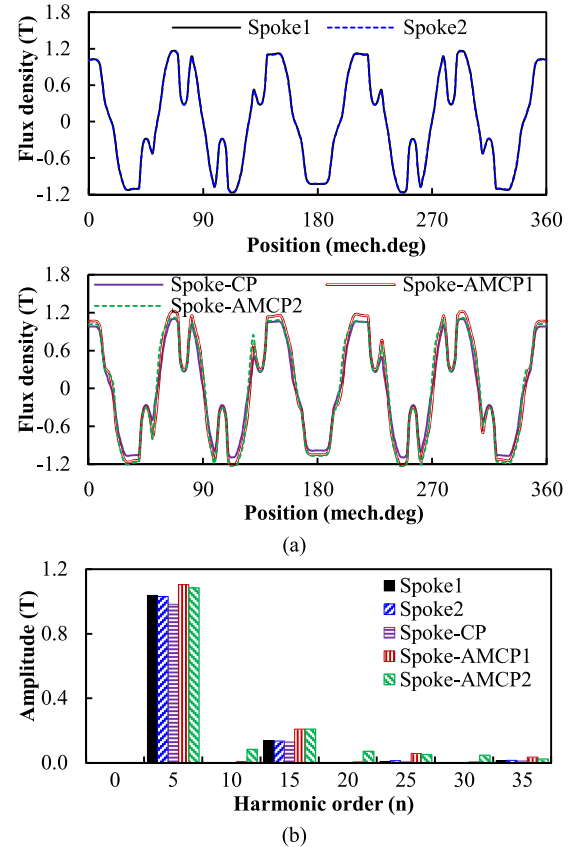


Fig. 7. Airgap flux density. (a) Waveforms. (b) Harmonics.

t_b for obtaining similar mechanical reliability to the Spoke1 machine. The Spoke-CP machine has the lowest fundamental airgap flux density because it has the most leakage flux in these machines, whereas the proposed Spoke-AMCP1 machine has the highest fundamental airgap flux density, which results from the strong flux-focusing effect and suppressed leakage flux.

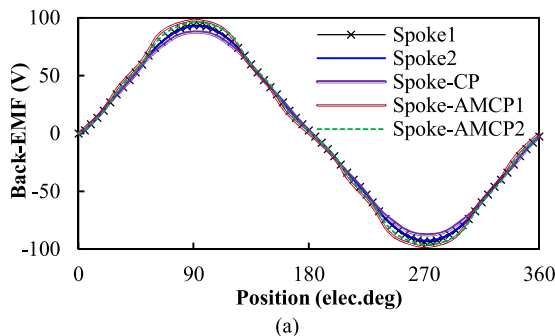
The Spoke-AMCP2 machine has slight low fundamental airgap flux density than the Spoke-AMCP1 machine due to the reduced PM volume. However, the PM utilization ratio of the Spoke-AMCP2 machine is higher than that of the Spoke-AMCP1 machine, as will be shown later. In addition, the even-order harmonics hardly exist in the airgap flux density of the Spoke-CP and Spoke-AMCP1 machines, which is benefit from the proposed pole-shaping method.

B. Back-EMF

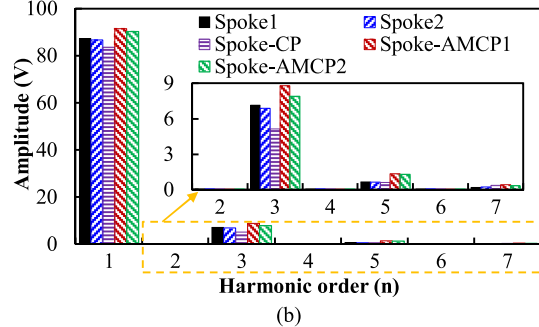
FE-predicted phase back-EMFs of the five machines and their harmonic contents are, respectively, shown in Fig. 8(a) and (b). It can be seen that the harmonic contents of these phase back-EMFs accord with the corresponding airgap flux densities. Although the Spoke-AMCP1 and Spoke-AMCP2 machines have slightly larger fifth and seventh harmonics of the phase back-EMF than the other three machines, they have lower torque ripple due to the higher average torque (fundamental phase back-EMF), as will be shown later.

TABLE V
TORQUE CHARACTERISTICS OF INVESTIGATED MACHINES

Items	Spoke1	Spoke2	Spoke-CP	Spoke-AMCP1	Spoke-AMCP2
6 th	0.03	0.03	0.06	0.05	0.05
12 th	0.05	0.05	0.04	0	0.03
T_{ave} (Nm)	4.12	4.09	3.94	4.23	4.19
T_{ave} [%]	100	99.3	95.6	102.7	101.7
ΔT_{p-p} (Nm)	0.15	0.14	0.16	0.11	0.13
T_{ripple} (%)	3.6	3.4	4.1	2.6	3.1
T_c (mNm)	20	21	22	26	16
V_m (cm ³)	17	17	17	17	16
η_m (Nm/cm ³)	0.242	0.241	0.232	0.249	0.262
η_m [%]	100	99.6	95.9	102.9	108.2



(a)



(b)

Fig. 8. Phase back-EMFs. (a) Waveforms. (b) Harmonics.

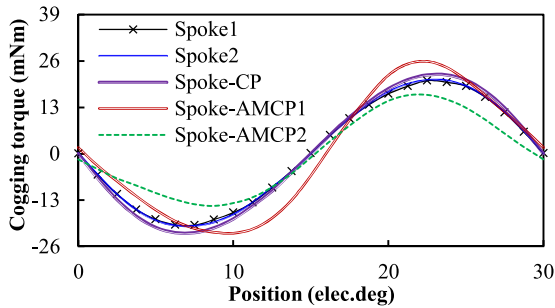
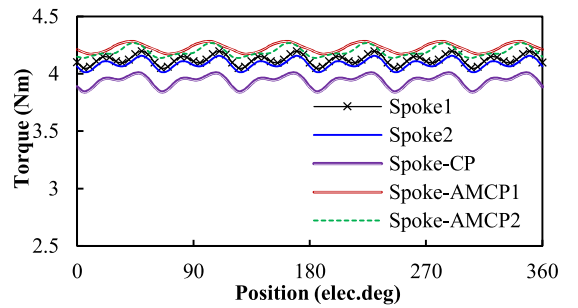


Fig. 9. Variation of cogging torques with rotor position.

C. Torque Characteristics

Fig. 9 shows the cogging torques of all these machines, and their peak values T_c are listed in Table V. Due to the same smallest common multiple between the stator slot number and the rotor pole-pair number, these machines have the same period

Fig. 10. Variation of electromagnetic torques with rotor position under $i_d = 0$.

of cogging torque. It can be seen that all these machines have small peak value of cogging torque, and the Spoke-AMCP2 has the lowest value in them.

Fig. 10 shows the electromagnetic torques of the five machines under $i_d = 0$ control, and their characteristics are listed in Table V, where T_{ave} is the average torque, ΔT_{p-p} is the peak-to-peak value of torque waveform, T_{ripple} is the torque ripple, V_m is the PM volume, and η_m is the PM utilization ratio (average torque per PM volume). It can be seen that the Spoke-AMCP1 and Spoke-CP machines, respectively, have the largest and lowest average torque in these machines, whereas the Spoke1 and Spoke2 machines have the similar average torque. Therefore, due to the same PM volume of the four machines (Spoke1, Spoke2, Spoke-CP, and Spoke-AMCP1), the Spoke-AMCP1 and Spoke-CP machines, respectively, have the highest and lowest PM utilization ratio. In addition, since the Spoke-AMCP2 machine has lower PM volume than the Spoke-AMCP1 machine, the Spoke-AMCP2 machine has the highest PM utilization ratio, which is $>8\%$ higher than the Spoke1, Spoke2, and Spoke-CP machines.

Meanwhile, it can be observed that the Spoke-AMCP1 and Spoke-AMCP2 machines has slight lower sixth harmonic torque than the Spoke-CP machine, and slight larger sixth harmonic torque than the Spoke1 and Spoke2 machines. Moreover, the Spoke-AMCP1 machine has no 12th harmonic torque. Together with the largest average torque, the Spoke-AMCP1 machine has the lowest torque ripple. In addition, although the 12th harmonic torque of the Spoke-AMCP2 machine is larger than that of the Spoke-AMCP1 machine, it is lower than that of the other three

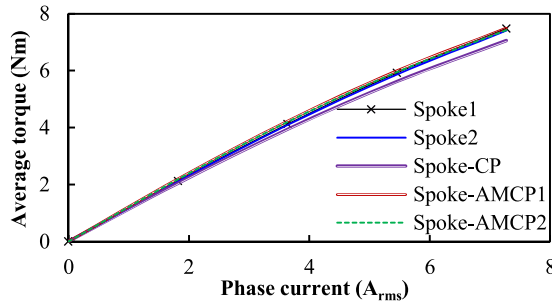


Fig. 11. Variation of average torque with armature current.

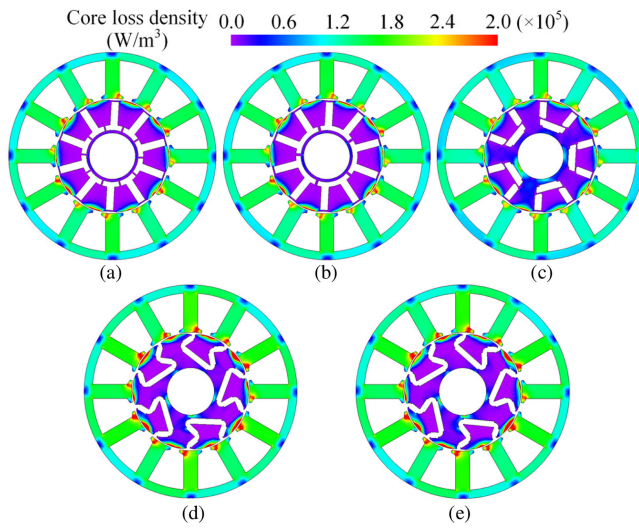


Fig. 12. Distribution of core loss density. (a) Spoke1. (b) Spoke2. (c) Spoke-CP. (d) Spoke-AMCP1. (e) Spoke-AMCP2. (1500 r/min, 3.6 A_{rms}).

machines. Consequently, the Spoke-AMCP2 machine obtains lower torque ripple than the Spoke1, Spoke2, and Spoke-CP machines.

Fig. 11 shows the variation of average torque with armature current for all these machines. It can be seen that the Spoke-CP and two Spoke-AMCP machines have inferior linearity of current-torque curve than the Spoke1 and Spoke2 machines. However, the Spoke-AMCP1 machine still obtains higher output torque and PM utilization ratio than the conventional machines.

D. Loss and Efficiency

The measured phase resistance is adopted to calculate the copper loss, which neglects the ac loss. Then, the copper loss is calculated to be 39.7 W at the rated current. The distributions of core loss density in these typical machines at rated current and speed are shown in Fig. 12. The iron loss P_{iron} (including eddy loss of stator core $P_{e,s}$, hysteresis loss of stator core $P_{h,s}$, eddy loss of rotor core $P_{e,r}$, hysteresis loss of rotor core $P_{h,r}$, PM eddy loss P_m), the electromagnetic power P_{em} , and the efficiency η of these machines are listed in Table VI.

It can be seen that the rotor core losses of all the machines are much lower than the stator core loss because the flux density

TABLE VI
LOSS AND EFFICIENCY OF INVESTIGATED MACHINES

Items	Spoke1	Spoke2	Spoke-CP	Spoke-AMCP1	Spoke-AMCP2
$P_{e,s}$ (W)	4.47	4.37	4.04	5.34	5.07
$P_{h,s}$ (W)	5.41	5.37	5.23	5.71	5.70
$P_{e,r}$ (W)	0.53	0.54	0.68	0.83	0.84
$P_{h,r}$ (W)	0.50	0.51	0.72	0.71	0.72
P_m (W)	0.10	0.10	0.04	0.02	0.03
P_{iron} (W)	11.02	10.89	10.71	12.61	12.37
P_{em} (kW)	0.65	0.64	0.62	0.66	0.66
η (%)	92.6	92.6	92.3	92.6	92.6

TABLE VII
PARAMETERS FOR FLUX-WEAKENING CAPABILITY

Items	Spoke1	Spoke2	Spoke-CP	Spoke-AMCP1	Spoke-AMCP2
ψ_{pm} (mWb)	111.3	110.4	106.4	116.5	115.0
L_d (mH)	10.8	10.9	11.7	12.2	12.1
I_{ch} (A)	10.3	10.1	9.1	9.5	9.5
k_f	0.35	0.36	0.40	0.38	0.38

distribution of rotor changes little over time. The Spoke-AMCP1 and Spoke-AMCP2 machines have larger stator core loss than other machines due to the highest airgap flux density. Moreover, the Spoke-CP, Spoke-AMCP1, and Spoke-AMCP2 machines have larger rotor core loss than Spoke1 and Spoke2 machines due to the more harmonics of armature field incurred by consequent topology. However, the iron losses of all these machines are much lower than the copper loss due to the low speed, i.e., 1500 r/min. Together with the enhanced output torque (output power), the Spoke-AMCP1 and Spoke-AMCP2 machines obtain the same level efficiency as the Spoke1 and Spoke2 machines.

E. Flux-Weakening Capability

Flux weakening is often performed for achieving wide constant power operation. Characteristic current I_{ch} , i.e., the ratio of PM flux linkage ψ_{pm} to the d -axis inductance L_d , is a key parameter for evaluating the flux-weakening capability k_f , which is given as

$$I_{ch} = \frac{\psi_{pm}}{L_d} \quad (3)$$

$$k_f = \frac{I_r}{I_{ch}} \quad (4)$$

The PM flux linkage ψ_{pm} , the d -axis inductance L_d , characteristic current I_{ch} , and flux-weakening capability k_f of all these investigated machines are listed in Table VII.

Although the reluctance torque is a few percent of the PM torque in the fractional slot concentrated winding spoke-type PM machines [9], all these machines are controlled based on the maximum torque per ampere (MTPA) in order to utilize the slight reluctance torque. Figs. 13 and 14 show the efficiency contour maps and power-speed curves of all these machines at the peak phase current of 7.2 A_{rms} and dc voltage of 220 V. It can be seen that the Spoke-AMCP1 and Spoke-AMCP2 machines

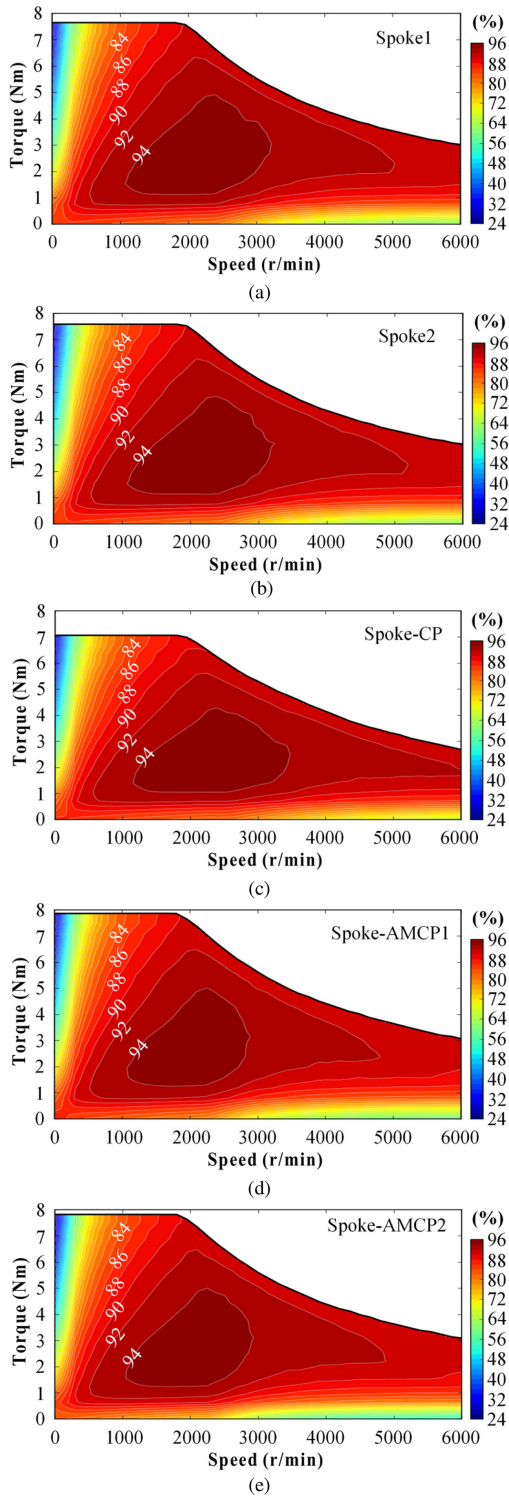


Fig. 13. Efficiency counter maps. (a) Spoke1. (b) Spoke2. (c) Spoke-CP. (d) Spoke-AMCP1. (e) Spoke-AMCP2. ($I_{\max} = 7.2 \text{ A}_{\text{rms}}$, $U_{\text{dc}} = 220 \text{ V}$).

have slightly better flux-weakening capability than the Spoke1 and Spoke2 machines due to the higher L_d . Moreover, the Spoke-AMCP1 and Spoke-AMCP2 machines have almost the same efficiency as the Spoke1, Spoke2, and Spoke-CP machines at low speed. However, they have slightly lower efficiency than

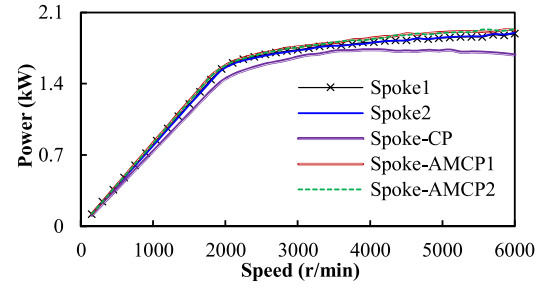


Fig. 14. Output power versus speed ($I_{\max} = 7.2 \text{ A}_{\text{rms}}$, $U_{\text{dc}} = 220 \text{ V}$).

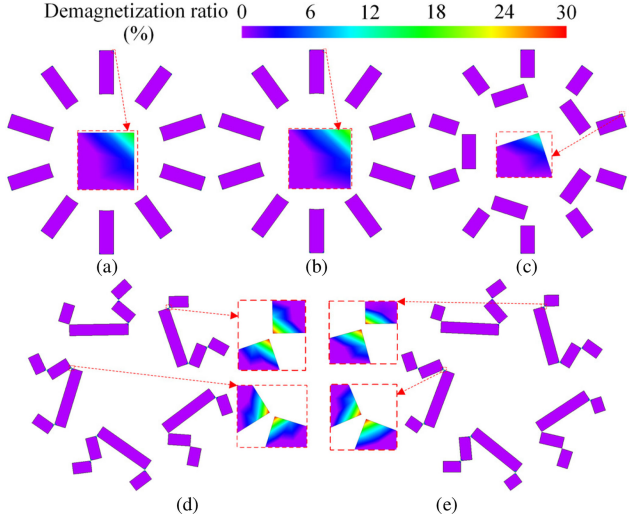


Fig. 15. Distributions of demagnetization ratio in PMs. (a) Spoke1. (b) Spoke2. (c) Spoke-CP. (d) Spoke-AMCP1. (e) Spoke-AMCP2.

the other machines due to the larger core losses at high speed. In spite of it, the two Spoke-AMCP machines have higher output power than the other machines during the full-speed region due to the improved torque capability.

F. Demagnetization Withstand Capability

Demagnetization analysis is an important concern for a new PM rotor topology. The irreversible demagnetization of PMs in these machines is investigated under overload ($i_d = -2\sqrt{2}I_{\text{rms}}$) when the PM temperature is 60° and the knee point of the demagnetization curve is $(-0.22 \text{ T}, -1044 \text{ kA/m})$. In order to evaluate the distribution and level of the demagnetization in PM, the demagnetization ratio k_d is defined as

$$k_d = \left(1 - \frac{B'_r}{B_r} \right) \times 100\% \quad (5)$$

where B_r and B'_r are the remanence of the PM before and after irreversible demagnetization, respectively.

The distributions of the demagnetization ratios of all these machines are shown in Fig. 15. For the Spoke1, Spoke2, and Spoke-CP machines, the irreversible demagnetization occurs in the edge of PM close to the airgap. For the Spoke-AMCP1 and Spoke-AMCP2 machines, the irreversible demagnetization

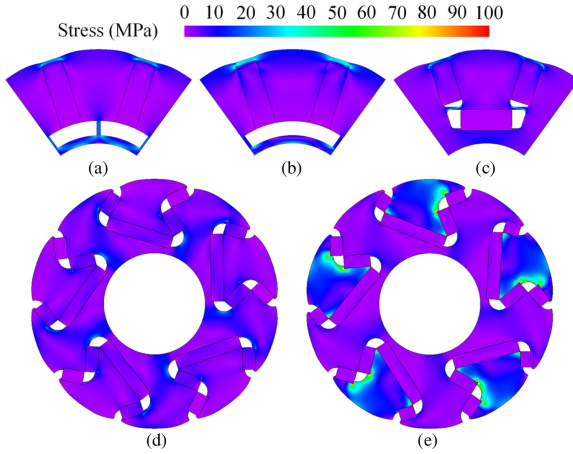


Fig. 16. Distributions of rotor stress. (a) Spoke1. (b) Spoke2. (c) Spoke-CP. (d) Spoke-AMCP1. (e) Spoke-AMCP2.

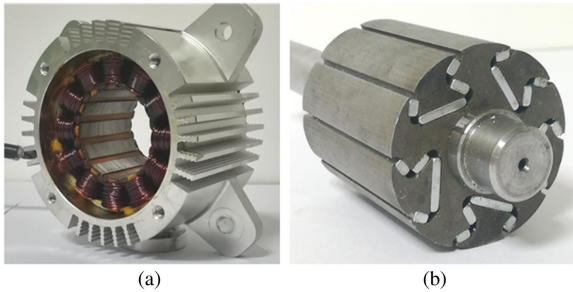


Fig. 17. Prototype. (a) Stator. (b) Rotor.

occurs in the adjacent edge of PMs. However, for all these machines, the area of the demagnetization is very little, which has negligible influence on the electromagnetic performance.

G. Rotor Stress

As an important concern, the mechanical strength of the proposed Spoke-AMCP rotor is investigated and compared with that of conventional Spoke-type rotors at the maximum speed (10 000 r/min). The mechanical properties of core and PMs are the same as [23, Table V]. The calculated rotor stress distributions of these rotors are shown in Fig. 16. It can be seen that the maximum stress occurs in the corners of the flux bridges and ribs for all the conventional Spoke-type rotors. For the Spoke-AMCP rotor, the location of the maximum stress is different with the PM parameters. More importantly, these results show that the Spoke-AMCP rotor can obtain sufficient safety margin due to its self-locking function.

IV. EXPERIMENTAL VERIFICATION AND DISCUSSION

The 12-slot/10-pole Spoke-AMCP1 machine has been prototyped and tested for the verification of previous analyses. Fig. 17(a) and (b) shows the photographs of the 12-slot stator and 10-pole Spoke-AMCP rotor, respectively. The main rotor core and separated cores are fabricated by wire cutting. The four PMs per pole-pair are first assembled with the main core, and then

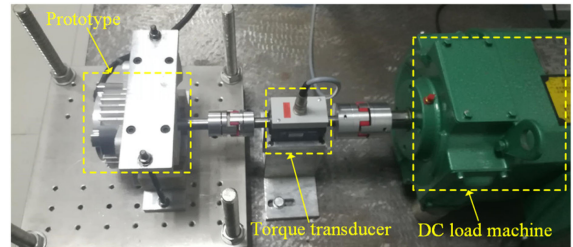


Fig. 18. Dynamic Test Platform.

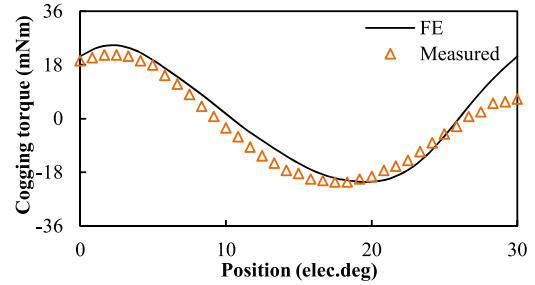


Fig. 19. Comparison of FE-predicted and measured cogging torques.

the segmented iron-pole is pushed in the rotor. In actual mass production, the main core and segmented poles can be connected by thin bridges (thinner than those of the conventional Spoke-type PM machines) for reducing the manufacturing complexity, and then the rotor core can be fabricated by silicon steel sheet, which is the same as the conventional Spoke-type PM machines. In other words, the Spoke-AMCP machine can have thinner bridges than the conventional Spoke-type PM machines because it can ensure the mechanical safety by its self-locking function.

Fig. 18 shows the platform for the dynamic test, in which a dc-motor-based dynamometer is adopted as a variable load and is used for the test of phase back-EMF. In addition, an encoder is employed to detect the rotor position of the prototype, while the phase current and torque are tested by the current probe and torque transducer, respectively. In order to consider the influences of the lamination factor (0.95) by silicon steel sheet (50W1300) and the working temperature on the difference between the predicted and measured results, the FE model adopts the active stack length (48.45 mm) and assumed working temperature (60°C) to predict the on-load performance.

Fig. 19 shows the FE-predicted and measured cogging torques, where the measured one is obtained by the static platform as reported in [21]. The large difference can be found between them. This is due to that the FE model assumes the perfect manufacture and assembly of the prototype machine. However, there are inevitably mechanical tolerances in manufacture and assembly deficiencies in practice. In particular, the machine has the separated rotor core, which makes the assembly errors to be bigger and, hence, increases the rotor eccentricity. Moreover, the cogging torque is very small (26 mN·m), which is more sensitive to these factors.

Fig. 20(a) shows the measured phase back-EMF waveforms at rated speed, and Fig. 20(b) shows the harmonics contents.

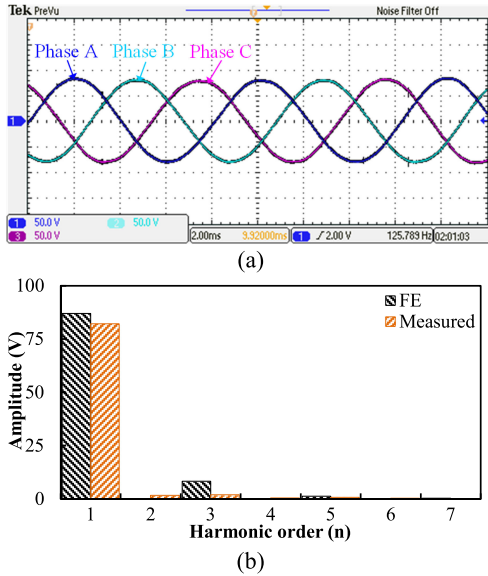


Fig. 20. Phase back-EMFs. (a) Measured waveform. (b) Harmonics of FE-predicted and measured ones.

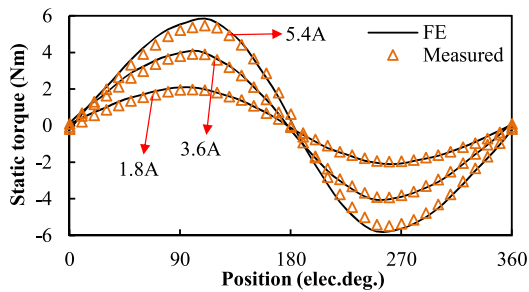


Fig. 21. Comparison of FE-predicted and measured static torques.

TABLE VIII
COMPARISON OF FE-PREDICTED AND MEASURED BACK-EMFS
AND TORQUES

Items	1 st Phase Back- EMF (V)	Torque (Nm)					
		Static (90 elec. deg.)			Steady		
		1.8A	3.6A	5.4A	1.8A	3.6A	5.4A
FE	87.05	2.09	3.97	5.53	2.05	3.91	5.53
Measured	82.22	1.95	3.80	5.22	1.94	3.75	5.20
Error (%)	5.5	6.7	4.3	5.6	5.4	4.1	6.0

It can be seen that the measured result has much lower third harmonic than the FE-predicted one. Fig. 21 shows the FE-predicted and measured static torques with rotor position, which is performed by supplying the current with $I_a = 0$ and $I_b = -I_c = I_{dc}$ into the three-phase windings. From above, both the measured phase back-EMF and static torques are lower than the FE-predicted ones, as listed in Table VIII. This mainly results from the neglected end effect in the ideal 2-D FE model.

The measured steady torque and current waveforms are shown in Fig. 22. Fig. 23 shows the variation of measured output torque with armature current, which is lower than the FE-predicted one, as listed in Table VIII.

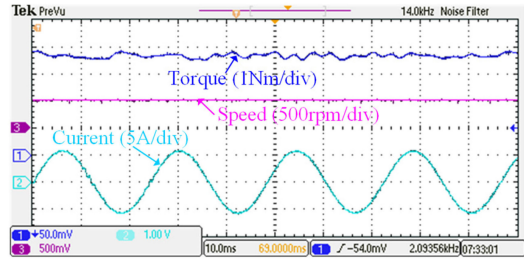


Fig. 22. Measured steady torque and current waveforms.

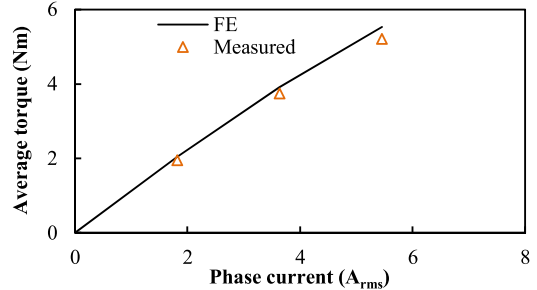


Fig. 23. Comparison of FE-predicted and measured output torques versus armature currents.

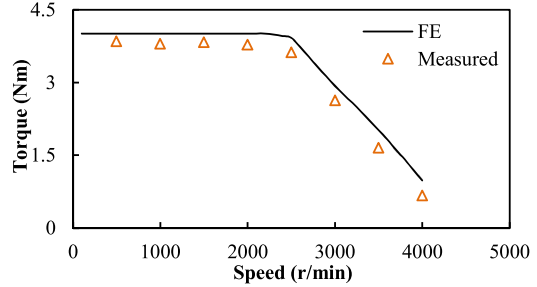


Fig. 24. Comparison of FE-predicted and measured torque-speed curves.

Fig. 24 shows the FE-predicted and measured torque-speed curves under rated current and dc voltage of 220&V. In general, all the measured results have good match with the FE-predicted ones.

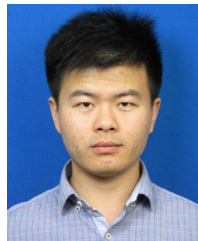
V. CONCLUSION

In order to improve the torque density, PM utilization ratio and flux-weakening capability of the Spoke-type PM machine simultaneously, the Spoke-AMCP rotor is proposed and investigated in this paper. Moreover, the pole-shaping method based on three-sectional arcs is proposed to suppress the harmonics of airgap flux density. Considering the complex structure, the FE analysis coupled with multiobjective GA is adopted to optimize the design. Then, the proposed Spoke-AMCP machine is compared with the existing Spoke1, Spoke2, and Spoke-CP machines on electromagnetic performance. It is demonstrated that the Spoke-AMCP machine obtains the largest output torque and highest PM utilization ratio in these machines due to the increased flux-focusing effect and reduced leakage flux resulting

from the elimination of flux bridges and ribs. Moreover, it obtains lower torque ripple, similar efficiency and higher output power during the full-speed region compared with the existing machines. All these indicate that the Spoke-AMCP machine can be a strong candidate for high-performance applications when PM utilization ratio is emphasized.

REFERENCES

- [1] K. T. Chau, C. C. Chan, and C. Liu, "Overview of permanent-magnet brushless drives for electric and hybrid electric vehicles," *IEEE Trans. Ind. Electron.*, vol. 55, no. 6, pp. 2246–2257, Jun. 2008.
- [2] Z. Q. Zhu and D. Howe, "Electrical machines and drives for electric, hybrid and fuel cell vehicles," *Proc. IEEE*, vol. 95, no. 4, pp. 746–765, Apr. 2007.
- [3] I. Boldea, L. N. Tutelea, L. Parsa, and D. Dorrell, "Automotive electric propulsion systems with reduced or no permanent magnets: An overview," *IEEE Trans. Ind. Electron.*, vol. 61, no. 10, pp. 5696–5711, Oct. 2014.
- [4] M. Kim *et al.*, "Torque density elevation in concentrated winding interior PM synchronous motor with minimized magnet volume," *IEEE Trans. Magn.*, vol. 49, no. 7, pp. 3334–3337, Jul. 2013.
- [5] K. I. Laskaris and A. G. Kladas, "Internal permanent magnet motor design for electric vehicle drive," *IEEE Trans. Ind. Electron.*, vol. 57, no. 1, pp. 138–145, Jan. 2010.
- [6] Q. Chen, G. Liu, W. Zhao, and M. Shao, "Nonlinear adaptive lumped parameter magnetic circuit analysis for spoke-type fault-tolerant permanent magnet motors," *IEEE Trans. Magn.*, vol. 49, no. 9, pp. 5150–5157, Sep. 2013.
- [7] Q. Chen, G. Liu, W. Zhao, L. Sun, M. Shao, and Z. Liu, "Design and comparison of two fault-tolerant interior-permanent-magnet motors," *IEEE Trans. Ind. Electron.*, vol. 61, no. 12, pp. 6615–6623, Dec. 2014.
- [8] M. Si, X. Y. Yang, S. W. Zhao, and S. Gong, "Design and analysis of a novel spoke-type permanent magnet synchronous motor," *IET Elect. Power Appl.*, vol. 10, no. 6, pp. 571–580, Jan. 2016.
- [9] E. Carraro, N. Bianchi, S. Zhang, and M. Koch, "Design and performance comparison of fractional slot concentrated winding spoke type synchronous motors with different slot-pole combinations," *IEEE Trans. Energy Convers.*, vol. 34, no. 3, pp. 2276–2284, Feb. 2018.
- [10] A. Fasolo, L. Alberti, and N. Bianchi, "Performance comparison between switching-flux and IPM machines with rare-earth and ferrite PMs," *IEEE Trans. Ind. Appl.*, vol. 50, no. 6, pp. 3708–3716, Nov./Dec. 2014.
- [11] C. L. Jeong and J. Hur, "A novel proposal to improve reliability of spoke-type BLDC motor using ferrite permanent magnet," *IEEE Trans. Ind. Appl.*, vol. 52, no. 5, pp. 3814–3821, Oct. 2016.
- [12] S. I. Kim, J. Cho, S. Park, T. Park, and S. Lim, "Characteristics comparison of a conventional and modified spoke-type ferrite magnet motor for traction drives of low-speed electric vehicles," *IEEE Trans. Ind. Appl.*, vol. 49, no. 6, pp. 2516–2523, Dec. 2013.
- [13] H. J. Kim, D. Y. Kim, and J. P. Hong, "Structure of concentrated-flux-type interior permanent-magnet synchronous motors using ferrite permanent magnets," *IEEE Trans. Magn.*, vol. 50, no. 11, Nov. 2014, Art. no. 8206704.
- [14] A. M. El-Refaie *et al.*, "Advanced high-power-density interior permanent magnet motor for traction applications," *IEEE Trans. Ind. Appl.*, vol. 50, no. 5, pp. 3235–3248, Sep./Oct. 2014.
- [15] M. Kimiaebeigi, R. Long, J. Widmer, and Y. Gao, "Comparative assessment of single piece and fir-tree-based spoke type rotor designs for low-cost electric vehicle application," *IEEE Trans. Energy Convers.*, vol. 32, no. 2, pp. 486–494, Jun. 2017.
- [16] W. Zhao, J. W. Kwon, X. Wang, T. A. Lipo, and B. I. Kwon, "Optimal design of a spoke-type permanent magnet motor with phase-group concentrated-coil windings to minimize torque pulsations," *IEEE Trans. Magn.*, vol. 53, no. 6, Jun. 2017, Art. no. 8104604.
- [17] Y. H. Jung, M. S. Lim, M. H. Yoon, J. S. Jeong, and J. P. Hong, "Torque ripple reduction of IPMSM applying asymmetric rotor shape under certain load condition," *IEEE Trans. Energy Convers.*, vol. 33, no. 1, pp. 333–340, Sep. 2018.
- [18] S. Ooi, S. Morimoto, M. Sanada, and Y. Inoue, "Performance evaluation of a high-power-density PMASynRM with ferrite magnets," *IEEE Trans. Ind. Appl.*, vol. 49, no. 3, pp. 1308–1315, May/Jun. 2013.
- [19] M. Kimiaebeigi *et al.*, "High-performance low-cost electric motor for electric vehicles using ferrite magnets," *IEEE Trans. Ind. Electron.*, vol. 63, no. 1, pp. 113–122, Jan. 2016.
- [20] S. U. Chung, J. M. Kim, D. H. Koo, B. C. Woo, D. K. Hong, and J. Y. Lee, "Fractional slot concentrated winding permanent magnet synchronous machine with consequent pole rotor for low speed direct drive," *IEEE Trans. Magn.*, vol. 48, no. 11, pp. 2965–2968, Nov. 2012.
- [21] J. Li and K. Wang, "Analytical determination of optimal PM-arc ratio of consequent-pole permanent magnet machines," *IEEE/ASME Trans. Mechatronics*, vol. 23, no. 5, pp. 2168–2177, Oct. 2018.
- [22] M. Onsal, Y. Demir, and M. Aydin, "A new nine-phase permanent magnet synchronous motor with consequent pole rotor for high-power traction applications," *IEEE Trans. Magn.*, vol. 53, no. 11, Nov. 2017, Art. no. 8700606.
- [23] J. Li, K. Wang, and C. Liu, "Torque improvement and cost reduction of permanent magnet machines with dovetailed consequent-pole rotor," *IEEE Trans. Energy Convers.*, vol. 33, no. 4, pp. 1628–1640, Dec. 2018.
- [24] L. L. Wu and R. H. Qu, "Comparison of conventional and consequent pole interior permanent magnet machines for electric vehicle application," in *Proc. 17th Int. Conf. Elect. Mach. Syst.*, Hangzhou, China, Oct. 2014, pp. 70–74.
- [25] J. Li, K. Wang, and C. Liu, "Comparative study of consequent-pole and hybrid-pole permanent magnet machines," *IEEE Trans. Energy Convers.*, vol. 34, no. 2, pp. 701–711, Jun. 2019.
- [26] K. Wang, J. Li, S. S. Zhu, and C. Liu, "Novel hybrid-pole rotors for consequent-pole PM machines without unipolar leakage flux," *IEEE Trans. Ind. Electron.*, vol. 66, no. 9, pp. 6811–6823, Sep. 2019.
- [27] M. M. Rahman, K. T. Kim, and J. Hur, "Design and optimization of neodymium-free spoke-type motor with segmented winding-shaped PM," *IEEE Trans. Magn.*, vol. 50, no. 2, pp. 865–868, Feb. 2014.
- [28] X. Ge, Z. Q. Zhu, J. B. Li, and J. T. Chen, "A spoke-type IPM machine with novel alternate airspace barriers and reduction of unipolar leakage flux by step-staggered rotor," *IEEE Trans. Ind. Appl.*, vol. 52, no. 6, pp. 4789–4797, Nov./Dec. 2016.
- [29] M. Onsal *et al.*, "Rotor design optimization of a new flux-assisted consequent pole spoke-type permanent magnet torque motor for low-speed applications," *IEEE Trans. Magn.*, vol. 54, no. 11, Jun. 2018, Art. no. 8206005.
- [30] W. B. Liu and T. A. Lipo, "Analysis of consequent pole spoke type vernier permanent magnet machine with alternating flux barrier design," *IEEE Trans. Ind. Appl.*, vol. 54, no. 6, pp. 5918–5929, Nov./Dec. 2018.
- [31] X. Ren, D. W. Li, R. H. Qu, Z. X. Yu, and Y. T. Gao, "Investigation of spoke array permanent magnet vernier machine with alternate flux bridges," *IEEE Trans. Energy Convers.*, Early access.



J. Li (S'18) received the B.Eng. degree in automation from Chengxian College, Southeast University, Nanjing, China, in 2013, and the M.S. degree in electrical engineering from Shanghai DianJi University, Shanghai, China, in 2016. Since 2016, he has been working toward the Ph.D. degree in electrical engineering with the Department of Electrical Engineering, Nanjing University of Aeronautics and Astronautics, Nanjing, China.

His research interests include the design and analysis of permanent-magnet and hybrid-excited machines.



K. Wang (M'13–SM'14) received the B.Eng. degree in electrical engineering from China Jiliang University, Hangzhou, China, in 2004, and the Ph.D. degree in electrical engineering from Zhejiang University, Hangzhou, China, in 2009.

From 2009 to 2010, he was with the Memorial University of Newfoundland, St. John's, NL, Canada, as a Postdoctoral Fellow. From 2010 to 2013, he was with The University of Sheffield, Sheffield, U.K. From 2013 to 2015, he was a Research Associate with the Sheffield Siemens

Wind Power Research Centre, Sheffield, U.K., and a Research and Development Engineer with Ansys Inc., Canonsburg, PA, USA. Since 2015, he has been with the College of Automation Engineering, Nanjing University of Aeronautics and Astronautics, Nanjing, China. His current research interests include the design and control of permanent-magnet machines.